Journal of Materials Chemistry A

PAPER

View Article Online
View Journal | View Issue

Cite this: J. Mater. Chem. A, 2014, 2, 6238

Muon studies of Li^+ diffusion in $LiFePO_4$ nanoparticles of different polymorphs†

Thomas E. Ashton,[a] Josefa Vidal Laveda,[a] Donald A. MacLaren,[b] Peter J. Baker,[c] Adrian Porch,[d] Martin O. Jones[c] and Serena A. Corr*[a]

Received 30th January 2014
Accepted 5th March 2014

DOI: 10.1039/c4ta00543k

www.rsc.org/MaterialsA

The lithium diffusion in nanostructured olivine $LiFePO_4$ has been investigated for the first time using muon spectroscopy (μSR). A microwave-assisted approach has been employed for nanoparticle preparation, where the choice of solvent is shown to play an important role in determining particle morphology and crystal chemistry. Two phases have been obtained: *Pnma* $LiFePO_4$ and the high pressure *Cmcm* phase. The Li^+ diffusion behaviour is strikingly different in both phases, with D_{Li} of 6.25×10^{-10} cm^2 s^{-1} obtained for *Pnma* $LiFePO_4$ in good agreement with measurements of bulk materials. In contrast, Li^+ diffusion is impeded with the addition of the high pressure *Cmcm* phase, with a lower D_{Li} of 3.96×10^{-10} cm^2 s^{-1} noted. We have demonstrated an efficient microwave route to nanoparticle synthesis of positive electrode materials and we have also shown μSR measurements to be a powerful probe of Li^+ diffusion behaviour in nanoparticles.

A Introduction

Olivine structured *Pnma* $LiFePO_4$ has been the focus of much attention for the development of efficient positive insertion electrodes, as it presents an economical and non-toxic option for a rechargeable Li-ion battery cathode material.[1–4] $LiFePO_4$ exhibits a high charge density, good cyclability and is complementary to most conventional polymer electrolytes. Recently, great efforts have been made in the development of nanostructured electrodes due to potential improvements in electrochemical performance, as their small size allows for shorter diffusion pathlengths while increased surface areas improve electrode–electrolyte interactions.[5,6]

Phase pure olivine materials can be obtained using conventional synthetic methods, such as solid-state ceramic routes, sol–gel routes and solvothermal methods.[7–11] While high temperature ceramic routes will often yield bulk materials, the choice of solvent in solvothermal reactions can often play a determining role in resulting particle morphology and size. One example of a class of materials finding increasing use as solvents for the preparation of electrode materials is the use of ionic liquids, where elegant control over resulting particle size and shape has recently been demonstrated for the case of the solvothermal synthesis of $LiFePO_4$ and $LiMnPO_4$.[12–14] In recent years, microwave-assisted solvothermal methods have appeared as a faster, efficient approach to inorganic materials.[15] For example, $LiMPO_4$ (M = Fe, Mn) has been prepared by using a benzyl alcohol approach after only 3 minutes at 180 °C.[16] Microwave routes to nanostructured Li_2FeSiO_4 and Li_2MnSiO_4 using a tetraethylene glycol solvent have also been reported,[17] while recently Nazar and co-workers have established a fast, microwave-assisted polyol route to the triplite $LiFeSO_4F$ phase with tetraethylene glycol.[18]

Here, we report the synthesis of nanoparticulate $LiFePO_4$ using a microwave-assisted solvothermal route. We show how the crystal chemistry and resulting morphology can be controlled by the solvent and iron starting materials employed. We employ two methods combined with microwave heating: a polyol synthesis and an ionothermal route. We also report, for the first time, on the diffusive nature of Li^+ through $LiFePO_4$ nanoparticles prepared in this manner using positive muon spin relaxation (μSR). The nature of Li^+ diffusion in $LiFePO_4$ continues to attract considerable attention. A number of methods already exist for the study of Li^+ diffusion, yet there is significant variation between the results obtained for D_{Li} in $LiFePO_4$ (ranging from $\sim 10^{-7}$ cm^2 s^{-1} from Mössbauer spectroscopy[19] to $\sim 10^{-14}$ cm^2 s^{-1} for galvanostatic intermittent titration techniques [GITT][20]). Recently, electrochemical methods employed for calculating Li^+ diffusion coefficients in thin film electrodes have raised questions due to differences caused by the nature of the diffusion, the electrode surface area and the smoothness of the electrode surface.[21–23] Theoretical

[a]School of Chemistry, University of Glasgow, Glasgow G12 8QQ, UK. E-mail: serena.corr@glasgow.ac.uk; Tel: +44 (0)141 3302274

[b]SUPA, School of Physics and Astronomy, University of Glasgow G12 8QQ, UK

[c]ISIS Pulsed Neutron and Muon Source, STFC Rutherford Appleton Laboratory, Harwell Science and Innovation Campus, Didcot, Oxfordshire OX11 0QX, UK

[d]Centre for High Frequency Engineering, School of Engineering, Cardiff University, Cardiff, CF24 3AA, UK

† Electronic supplementary information (ESI) available: XRD patterns of $LiFePO_4$ products obtained for increasing temperatures for (a) ethylene glycol and (b) ionic liquid. See DOI: 10.1039/c4ta00543k

studies have found that, for $LiFePO_4$, Li^+ diffusion is confined to a curved 1-dimension in the [010] direction, with D_{Li} estimates of 10^{-8} cm^2 s^{-1}.[24–26] This 1-dimensional diffusion has been shown experimentally using a combination of neutron diffraction and maximum entropy methods.[27] Activation barriers for Li^+ and electron mobility have also been investigated experimentally using NMR and impedance analysis.[28,29]

μSR has previously been employed as a sensitive probe for magnetic ordering and also in the investigation of dynamic sample effects.[30] It has also been successfully applied to the study of Li^+ diffusion in a number of Li-ion battery materials including lithium metal oxides and ternary lithium nitridometallates, where the Li^+ diffusion perturbs the muon environment.[31–34] μSR has been shown to reliably determine D_{Li} values for Li_xCoO_2, with values obtained close to theoretically predicted values.[32,35] Recently, the use of μSR as a probe to study Li^+ diffusion in olivines has also been demonstrated for bulk olivine materials, including bulk $LiFePO_4$.[36–38]

Herein, we examine the Li^+ diffusion in nanoparticulate *Pnma* $LiFePO_4$ and the high pressure *Cmcm* $LiFePO_4$ phase using μSR for the first time. We observe a thermally activated Li^+ hopping regime for nanostructured *Pnma* $LiFePO_4$, similar to measurements obtained for bulk samples, demonstrating the reliability of this technique for the study of Li^+ diffusion. We also examine muon diffusion of the *Cmcm* $LiFePO_4$ polymorph for the first time in a mixed phase sample of *Pnma* $LiFePO_4$/*Cmcm* $LiFePO_4$.

B Synthesis

Powder samples of $LiFePO_4$ were prepared by grinding LiH_2PO_4 (0.263 g; 2.54 mmol) and $FeC_2O_4 \cdot 2H_2O$ (0.456 g; 0.254 mmol) in an agate mortar for 10 min and adding to 10 ml of either ethylene glycol (Sample LFP-EG1; Alfa Aesar, 99%) or 1-ethyl-3-methyl imidazolium trifluoromethanesulfonate (EMI-TFMS) (Sample LFP-IL; Solvionic, 99.5%) in 35 ml glass reaction vessels. The mixtures were stirred for 20 minutes before irradiation with microwaves in a CEM Discover SP microwave synthesiser (2.45 GHz) for 3 hours at 250 °C. The products were washed with water (2 × 20 ml), ethanol (2 × 20 ml) and acetone (20 ml), before drying in a vacuum oven at 80 °C overnight. The pale green powders were characterised by X-ray diffraction (XRD) (PANalytical X'Pert powder diffractometer) and scanning electron microscopy (SEM) (Carl Zeiss Sigma variable pressure analytical SEM). SEM samples were prepared on adhesive stubs and coated using a plasma sputter coater with a 99 : 1, Au : Pt target to avoid charging feedback. Transmission electron microscopy (TEM) was performed on a JEOL ARM instrument, operated at 200 keV. TEM samples were prepared by dispersing the sample in ethanol and dropping the suspension onto an amorphous holey carbon coated grid.

Muon spectroscopy

Spin polarised positive muons were implanted into $LiFePO_4$ samples, where they stop at interstitial sites and decay with a mean lifetime of 2.2 μs. Whilst implanted in the sample, the muon spin direction is affected by the local magnetic field at the stopping site. When the muon decays into a positron and two neutrinos, the positron is preferentially emitted in the direction of the muon spin at the instant of decay. The muon spin polarisation can be followed as a function of time by measuring the asymmetry in the count rate of the decaying positrons, $A(t)$, in two banks of detectors on opposite sides of the sample; (essentially, we monitor the muon's spin through its daughter positron).

μSR experiments were carried out at the ISIS pulsed muon and neutron source, using the EMU instrument and data were analysed using the WIMDA program. The samples were prepared by transferring the powders of $LiFePO_4$ (approximately 1 g) into titanium sample holders with a titanium foil window. Ti depolarises muons very weakly and so gives an easy-to-subtract background. In order to probe the lithium diffusion behaviour in two of our samples, we measured a temperature range of 100 K to 400 K at 10 K increments and at 0 G and applied longitudinal fields of 5 and 10 G. Multiple magnetic field measurements give more reliable determinations of simultaneously fitted parameters since it allows greater investigation of how the field distribution experienced by the muon is decoupled by the field applied parallel to the initial muon spin polarisation.

C Results and discussion

Microwave synthesis of nanoparticulate $LiFePO_4$

Ethylene glycol and EMI-TFMS were chosen as solvents for the preparation of $LiFePO_4$ nanoparticles for two reasons:

(a) Choice of solvent has been previously shown to heavily influence the resulting nanoparticle shape.[39]

(b) Both solvents are high boiling point solvents (ethylene glycol boils at 196 °C; EMI-TFMS has a decomposition temperature of 340 °C) with dipole moments which can interact with incoming microwaves to uniformly heat reactants.

Our synthetic approach takes advantage of a solvent's ability to efficiently absorb microwave energy and convert this into heat through the dielectric heating effect.[40] A material's dielectric properties can be described by its complex relative permittivity $\varepsilon = \varepsilon_1 - i\varepsilon_2$, which depends on both frequency and temperature. The real part ε_1 (more precisely, the quantity $\varepsilon_1 - 1$) is a measure of the ability of the material to be polarized by an electric field, and the imaginary part ε_2 is a measure of the efficiency with which the material converts electric field energy into heat. Assuming a uniform internal electric field of magnitude E within a sample of volume V, the time-averaged power dissipated P at some frequency f can be written as $P = \pi\varepsilon_2\varepsilon_0 f E^2 V$.

In order to assess the behaviour of the solvents we have employed in greater detail, we measured the microwave dielectric properties of ethylene glycol and the ionic liquid EMI-TFMS. Measurements were taken in the range 0.01 GHz to 10 GHz using a broadband coaxial probe connected to a microwave network analyser (N5232A PNA-L, Agilent Technologies).[41] All measurements were taken at a constant temperature of 27.5 °C and values of complex permittivity were verified using a TM_{010} microwave cavity operating at 2.45 GHz.[42] Results for the

frequency dependence of the complex permittivity of both liquids are shown in Fig. 1(a) and (b). We find that ethylene glycol behaves close to that of a classical Debye liquid[43] of static permittivity $\varepsilon_s = 37.8 \pm 0.4$ and relaxation frequency of 1.57 ± 0.01 GHz. EMI-TFMS, on the other hand, behaves as a liquid with finite electrical conductivity, whose imaginary (*i.e.* lossy) permittivity ε_2 exhibits the expected frequency variation below about 1 GHz of $\varepsilon_2 \approx \sigma/2\pi\varepsilon_0 f \propto 1/f$. From this, we deduce a dc electrical conductivity of $\sigma = 0.96 \pm 0.01$ S m^{-1}.

Some numerical values of complex permittivity of both liquids at spot frequencies of importance for microwave heating applications (namely 915 MHz, 2.45 GHz and 5.8 GHz) are shown in Table 1. The results obtained for ethylene glycol compare well with previously reported values.[44] Note that the errors quoted in our data are systematic errors of around ±1% associated with the simple quasi-static model[41] used to model the aperture admittance of the coaxial probe to convert microwave reflectance data into complex permittivity values. We find that both solvents have large measured values of ε_2, confirming their effectiveness as microwave absorbers. In Fig. 2 we plot the rms power dissipated P (expressed in W cm^{-3} of solvent) calculated for a fixed internal electric field of 10 kV m^{-1}, as is typical in a microwave heating application, using our measured complex permittivities shown in Fig. 1. We find that that the dissipated power densities are 72 and 95 W cm^{-3} at 2.45 GHz for EMI-TFMS and ethylene glycol, respectively, which are sufficient to drive the high temperatures required for our reactions.

In a typical synthesis, stoichiometric amounts of iron precursor and LiH_2PO_4 were mixed with 10 ml solvent for 20 min at 30 °C before a heat treatment in the microwave chamber at 250 °C for 3 hours. The results from three experiments are presented here: (1) LFP_EG1 from iron oxalate dihydrate, LiH_2PO_4 and ethylene glycol solvent, (2) LFP_EG2 from iron acetylacetonate, LiH_2PO_4 and ethylene glycol (note, temperature is 220 °C here) and (3) LFP_IL from iron oxalate dihydrate, LiH_2PO_4 and ionic liquid EMI-TFMS solvent.

Table 1 Numerical values for the real part ε_1 and imaginary part ε_2 of the complex relative permittivity ε for the two solvents used in the microwave reactions, measured at 27.5 °C and at the industrially important heating frequencies of 915 MHz, 2.45 GHz and 5.8 GHz

	915 MHz	2.45 GHz	5.8 GHz
Ethylene glycol	$\varepsilon_1 = 29.4 \pm 0.3$, $\varepsilon_2 = 13.3 \pm 0.1$	$\varepsilon_1 = 16.0 \pm 0.2$, $\varepsilon_2 = 14.0 \pm 0.1$	$\varepsilon_1 = 9.0 \pm 0.1$, $\varepsilon_2 = 9.0 \pm 0.1$
EMI-TFMS	$\varepsilon_1 = 14.0 \pm 0.1$, $\varepsilon_2 = 21.8 \pm 0.2$	$\varepsilon_1 = 11.6 \pm 0.1$, $\varepsilon_2 = 10.6 \pm 0.1$	$\varepsilon_1 = 9.4 \pm 0.1$, $\varepsilon_2 = 6.6 \pm 0.1$

XRD patterns collected for each dried powder sample are shown in Fig. 3. For sample LFP1_EG with iron oxalate as a starting material and ethylene glycol as a solvent, a two-phase system is found with the pattern plotted in Fig. 3(a) matched to *Pnma* $LiFePO_4$ and a high pressure $LiFePO_4$ phase which crystallizes in the *Cmcm* space group. Heating this sample in a tube furnace under Ar at 600 °C for one hour completely transforms the high pressure phase to *Pnma* $LiFePO_4$. This high pressure *Cmcm* phase has been realised before by García-Moreno and coworkers at high pressures (tens of kbar) and temperatures (hundreds of degrees).[45] Very recently Niederberger and coworkers have observed this phase at much lower reaction temperatures and times (195 °C, 3 min) for a nonaqueous microwave synthesis, whereby a change in the benzyl alcohol–2-pyrrolidinone solvent ratio can be used to tailor the phase obtained.[46] In our experiments, the solvent volume is held

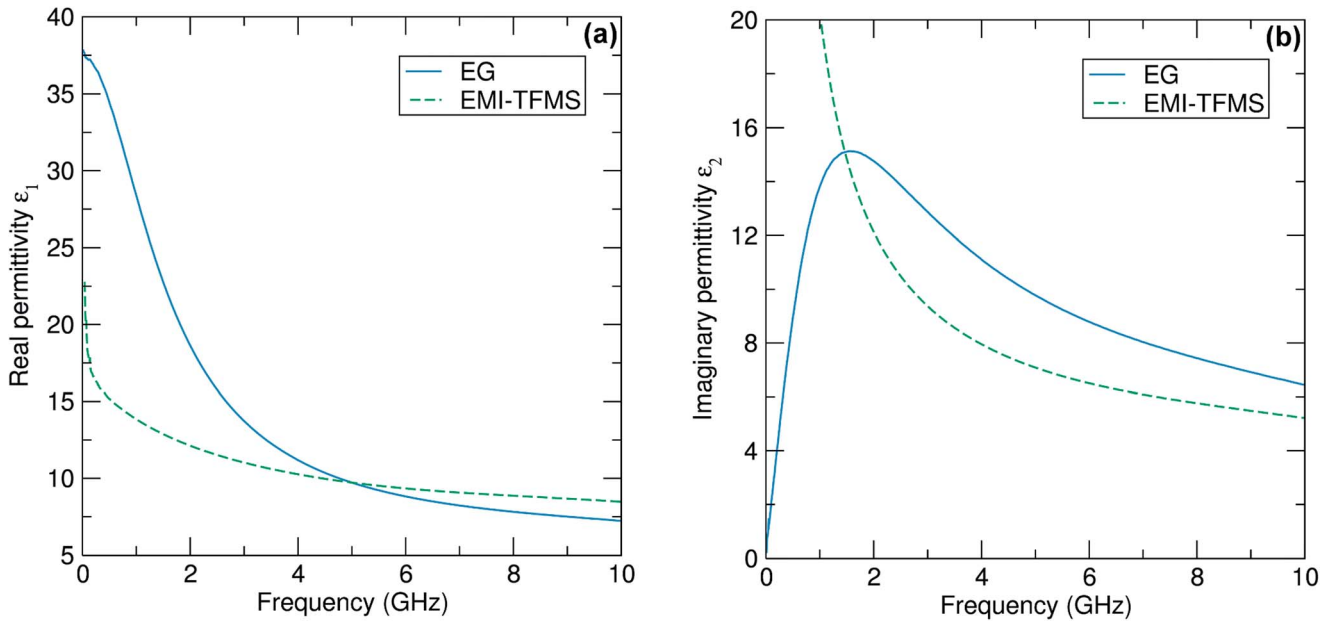

Fig. 1 (a) Experimental data for the real part ε_1 of the complex permittivity ε measured as a function of frequency for the polar liquid ethylene glycol (EG) and the ionic liquid EMI-TFMS. (b) The same plot, only this time for the imaginary part ε_2. No errors bars are shown but all data are subject to a systematic error of ±1% imposed by the aperture module of the coaxial probe used to extract the permittivity data.[41]

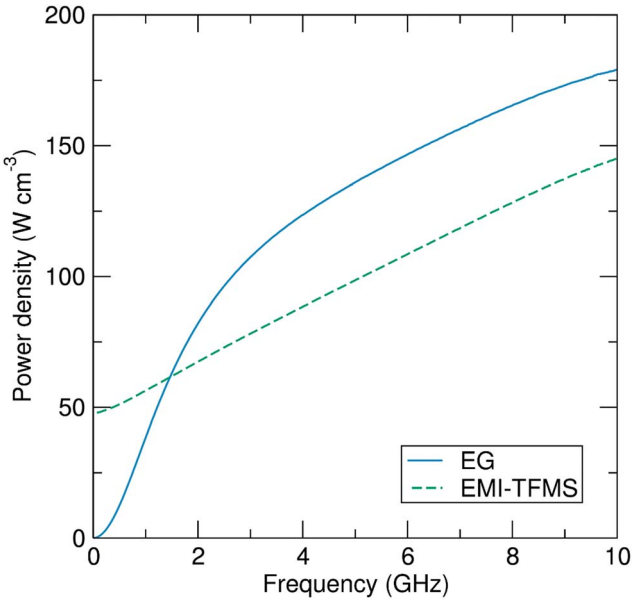

Fig. 2 The rms dissipated power density P (expressed in W cm^{-3}), calculated from the permittivity data of Fig. 1 for a uniform internal electric field of magnitude 10 kV m^{-1}, plotted as a function of frequency.

constant while the solvent itself is changed. Using a controlled synthesis, we can monitor the vessel pressure during synthesis. For the LFP_EG1 reaction, the observed pressure is approximately 5.86 bar once the reaction temperature of 250 °C is reached. This build-up of pressure is due to the removal of the waters of crystallisation from the iron starting material, which occurs between 170 °C and 230 °C.[47] We believe it is this change in pressure which drives the formation of the high pressure phase in the ethylene glycol reaction. By employing $Fe(acac)_3$ which has no water of crystallisation instead of $Fe(C_2O_4)\cdot 2H_2O$, we can obtain pure, single phase *Pnma* $LiFePO_4$ at 220 °C using an ethylene glycol solvent. The X-ray pattern of this sample, LFP_EG2, was fit by Rietveld profile analysis to the orthorhombic *Pnma* $LiFePO_4$ structure and is shown in Fig. 4(a). The solubility of starting materials is also different, with $Fe(acac)_3$ more soluble in ethylene glycol than the oxalate salt, as observed by the deep red colour of the solution prior to microwave treatment. The nature of the solvent is also of great importance in determining what phase is obtained, as demonstrated by the ionic liquid sample, LFP_IL. Using $Fe(C_2O_4)\cdot 2H_2O$ as a starting material and EMI-TFMS as solvent, which has a greater dissipated power density than ethylene glycol, single phase *Pnma* $LiFePO_4$ is obtained after 3 hours [Fig. 4(b)]. We have also studied the effect of reaction temperature on the phase obtained. For increasing reaction temperatures using ethylene glycol as a solvent and an iron oxalate starting material, we observe a two phase product made up of α- and β-$LiFePO_4$ even up to reaction temperatures of 300 °C (see XRD patterns in ESI, Fig. S1a†). In the case of EMI-TFMS as a solvent, we do not see the formation of the β-$LiFePO_4$ phase and only obtain α-$LiFePO_4$ at temperatures above 250 °C (see XRD patterns in ESI, Fig. S1b†). We are currently investigating the use of several commercial and tailored precursors to examine the effect of starting material and solvent on crystal chemistry in greater detail.

SEM images taken of dried powders of LFP_EG1 and LFP_IL reveal a dependence of particle morphology on the choice of solvent. In the case of LFP_EG1, large platelets are noted, with a typical platelet diameter of 6 μm. The thickness of these platelets is of the order of 20 nm and they appear as clusters of stacked particles as shown in Fig. 5(a). A dramatic difference is

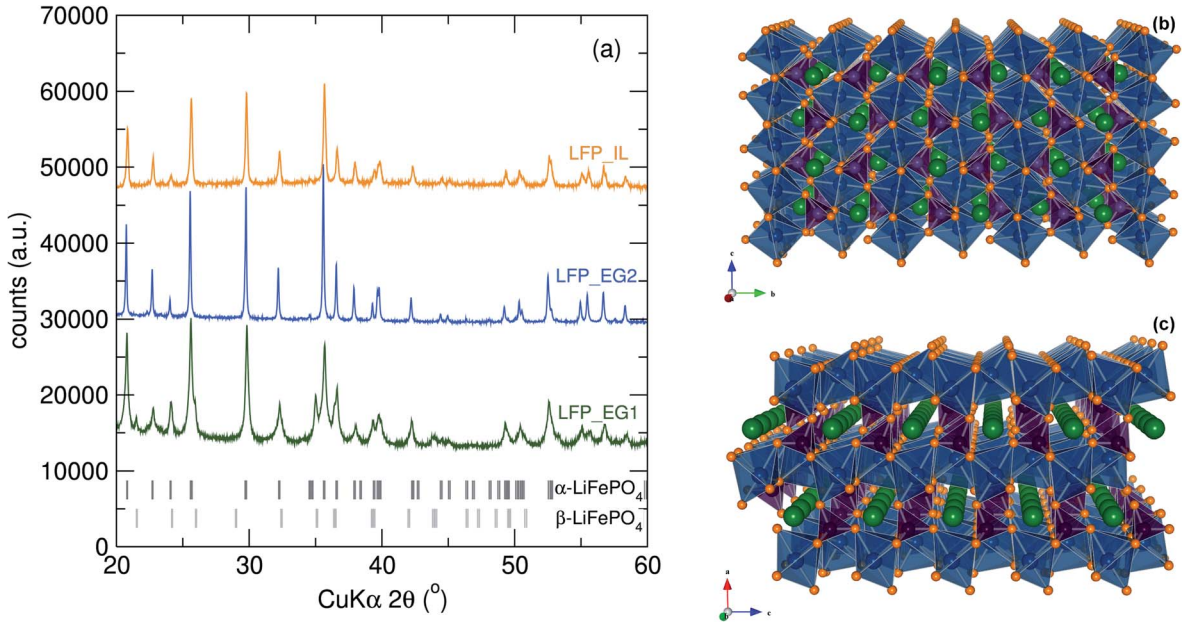

Fig. 3 (a) XRD data for LFP_EG1 reveals this is a two-phase system, comprising the *Pnma* structured $LiFePO_4$ (α-$LiFePO_4$) and the high pressure *Cmcm* phase (β-$LiFePO_4$). These phases are depicted in (b) *Cmcm* high pressure $LiFePO_4$ and (c) *Pnma* $LiFePO_4$.

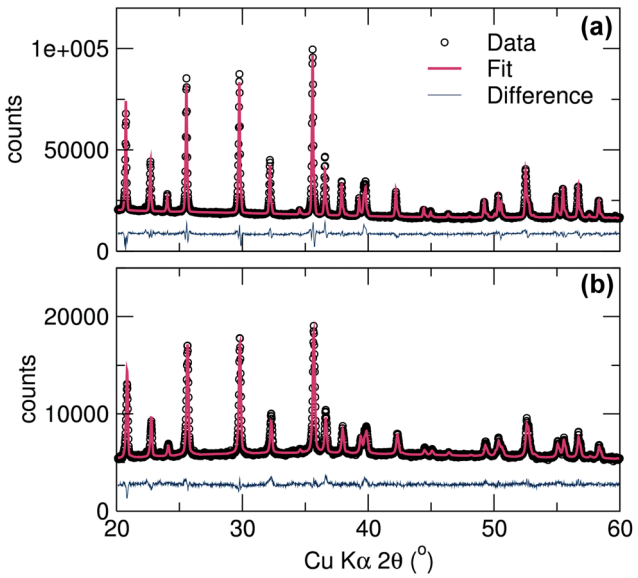

Fig. 4 Rietveld analysis was performed on single phase materials (a) LFP_EG2 [R_{wp} 14.8%, R_{exp} 4.15%, $a = 10.327$ Å, $b = 5.999$ Å, $c = 4.697$ Å] and (b) LFP_IL [R_{wp} 14.3%, R_{exp} 8.12%, $a = 10.327$ Å, $b = 6.003$ Å and $c = 4.693$ Å].

noted for the LFP_IL sample, where more nanoparticulate material, which often adopts geometric forms, is found to form under the same reaction conditions. The typical particle size in this case is 200 nm and in some cases the particles appear faceted [Fig. 5(b)]. High resolution TEM images confirm the highly crystalline nature of the LFP_IL sample [Fig. 5(d)], with lattice spacings consistent with *Pnma* $LiFePO_4$. Larger, sheet-like particles are again observed for the LFP_EG1 sample [Fig. 5(c)].

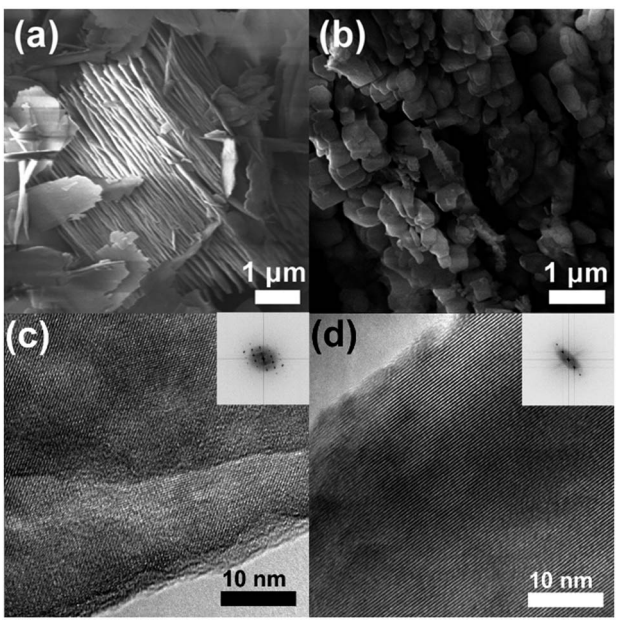

Fig. 5 SEM and TEM images of (a and c) LFP_EG1 and (b and d) LFP_IL, respectively. Large, stacked platelets and rods, with a typical thickness of 20 nm are noted for the EG1 sample, while more crystalline particles are seen for the IL sample. Long-range crystallinity throughout particles of both samples was confirmed by HRTEM images, with (inset) Fourier transforms demonstrating long-range crystallographic ordering (c and d).

μSR studies of Li^+ diffusion in nanoparticulate $LiFePO_4$

In terms of structure, the *Pnma* $LiFePO_4$ phase is characterised by open channels running in the *b*-direction through which Li^+ ions can diffuse during electrochemical cycling, as shown in Fig. 3(c). The structure of the *Cmcm* phase, shown in Fig. 3(b), is made up of rows of edge-sharing octahedral along the *c* axis, with PO_4 and LiO_4 tetrahedra running in the *a* direction.[45] As demonstrated previously, the major structural difference between these polymorphs is in the Li–Li distances, with the high pressure phase increasing to a point at which the lithium hopping mechanism is no longer viable.[46] The electrochemical properties of this phase have been investigated and it has been shown to be electrochemically inactive, with theoretical predictions in agreement with experiment.[45,46]

In order to probe the Li^+ diffusion in the pure *Pnma* and *Cmcm*-containing nanosized $LiFePO_4$ samples prepared here, we recorded μSR data at zero field (ZF) and applied longitudinal fields (LF) of 5 G and 10 G. The typical raw data obtained for the LFP_IL sample, recorded at 300 K, are shown in Fig. 6. The initial positron asymmetry, regardless of applied field, is approximately 17%. These measurements, which are taken above the antiferromagnetic ordering at T_N (LFP_IL, 51 K; LFP_EG, 49 K), contain a fast initial relaxation likely due to interactions with the paramagnetic iron moments and a slow relaxation from interactions with nuclear magnetic fields from ^{7}Li, ^{6}Li and ^{31}P. By applying a longitudinal field parallel to the

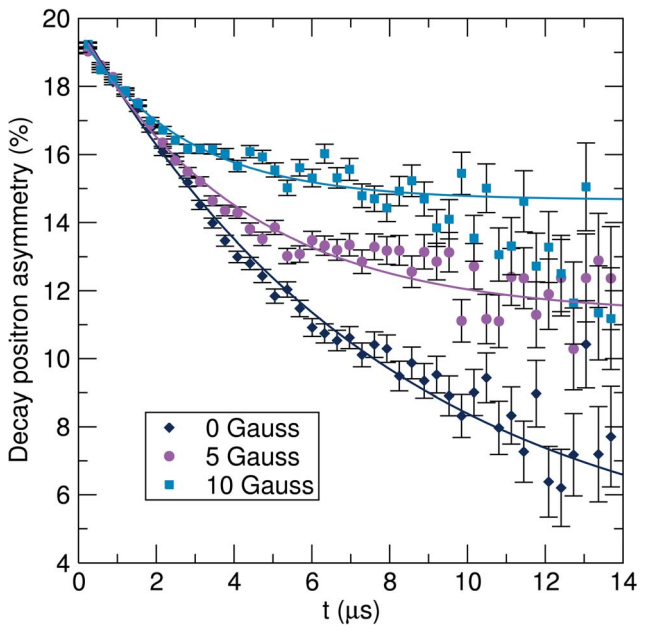

Fig. 6 Raw μSR data for LFP_IL collected at 300 K at zero field (ZF) [diamonds] and applied longitudinal fields of 5 G [circles] and 10 G [squares].

direction of the beam, any interactions between the muon and the local nuclear magnetic field distribution that it probes can be eliminated. Fig. 6 demonstrates this decoupling, where it can be seen that the application of progressively larger LF (from 5 G to 10 G) reduces this slower relaxation rate. Similar observations have been reported for bulk $LiFePO_4$.[36–38]

In order to probe the Li^+ diffusion dynamics in our samples, data were collected over a temperature range of 100 K to 400 K at ZF and LF of 5 G and 10 G. All data were fit using three parameters: a combination of an exponentially relaxing signal to account for the initial fast relaxation from the iron magnetic moments, a baseline asymmetry and an exponentially relaxing dynamic Kubo–Toyabe function,[30] which has been modified to account for fluctuations due to muon or lithium diffusion and can be employed for an assumed Gaussian distribution of local fields.[48] From these fits, we can extract parameters which provide us with insight into the Li^+ diffusion mechanism in our materials. In Fig. 7 and 8, we show the values of ν, the field fluctuation rate, and Δ, the local field distribution at the muon stopping site, for data collected over the full temperature range. Data extracted for the single phase $LiFePO_4$ sample LFP_IL are shown in Fig. 7. The values obtained for Δ are very similar to those observed for bulk $LiFePO_4$ samples reported previously, *i.e.* a low temperature plateau followed by a smooth decrease to higher temperatures [Fig. 7(b)]. In the case of the fluctuation rate, ν, we again observe similar behaviour as seen for bulk $LiFePO_4$. From 160 K, we see a steady increase until 230 K after which there is a sharp drop. The observed decrease in ν above 240 K likely results from the Li^+ diffusion being too fast for μ^+SR.[38] To evaluate the diffusion coefficient for Li^+, we consider

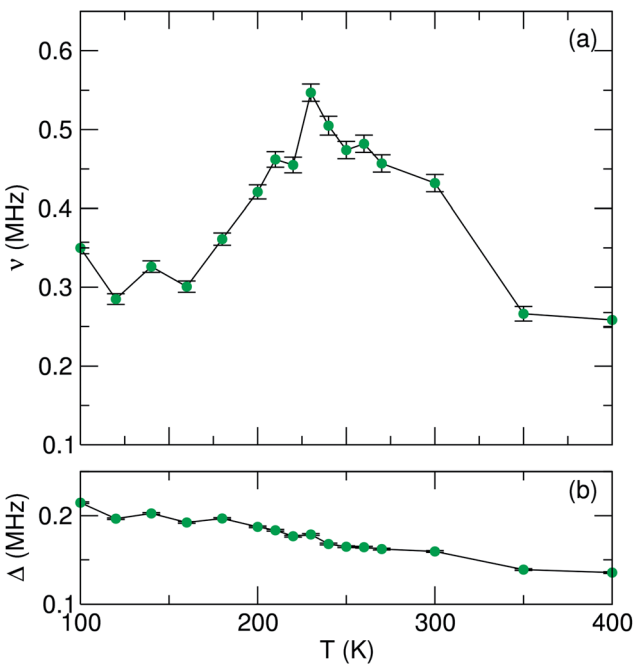

Fig. 7 Temperature dependence of (a) fluctuation rate (ν) and (b) field distribution width (Δ) parameters derived from fitting μSR data to a dynamic Kubo–Toyabe function for the LFP_IL sample, measured from 100 K to 400 K.

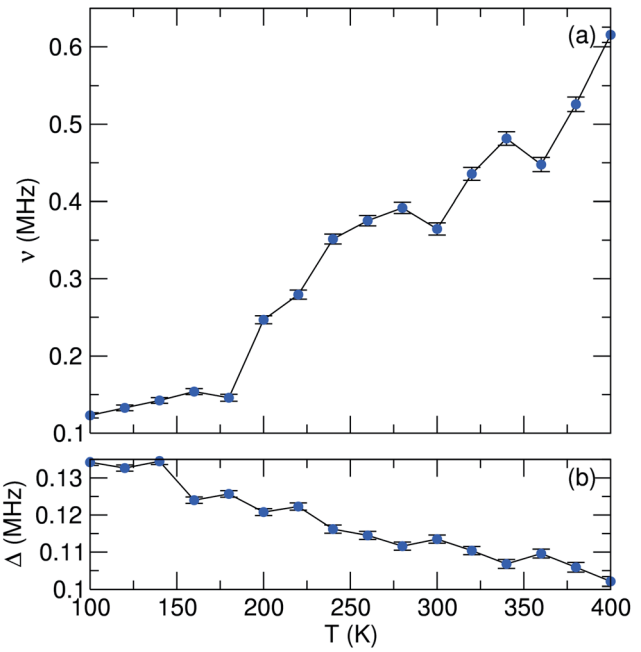

Fig. 8 Temperature dependence of (a) fluctuation rate (ν) and (b) field distribution width (Δ) parameters derived from fitting μSR data to a dynamic Kubo–Toyabe function for the LFP_EG1 sample, measured from 100 K to 400 K.

only jumps of Li^+ to interstitial sites and we take the primary hopping axis to be in the *b*-direction. The distance travelled for each hop will be therefore $b/2$, giving an estimation of the Li^+ diffusion coefficient, D_{Li}, from $b^2\nu/4$. For the LFP_IL sample, we can extrapolate fits of D_{Li} *versus* $1/T$ to obtain a Li^+ diffusion coefficient at 300 K of 6.25×10^{-10} cm^2 s^{-1}. This is in close agreement to bulk sample measurements.[36,37]

To determine the activation energy, we plot an Arrhenius fit to ν over the thermally activated region to give an estimated E_a of 58 meV for the LFP_IL sample. This value is close to the bulk reported value from Baker *et al.* who employed a Keren fitting function to data and obtained an E_a value of 60 meV.[36] For bulk $LiFePO_4$ prepared by ceramic methods and using similar Kubo–Toyabe fitting methods, Sugiyama *et al.* have found E_a values close to 100 meV.[37,38] The similarities in values obtained demonstrate the robustness of this method for determining Li^+ diffusion behaviour.

In the case of the LFP_EG1 sample (Fig. 8), we initially observe similar behaviour to the LFP_IL case, albeit with smaller Δ and ν values. An increase in ν is noted with increasing temperature, but now a decrease after 230 K is not seen. Instead, a steady increase is observed over the remaining temperature range. Given that this is a two phase system comprising *Pnma* and *Cmcm* $LiFePO_4$, it is reasonable to assume that the initial increase up to 230 K is due to Li^+ diffusion, similar to the case of the LFP_IL sample and previous observations for bulk samples. Previous reports on the high pressure *Cmcm* phase have shown that this phase is inactive electrochemically, with DFT simulations establishing the poor Li^+ mobility, with no hopping observed for the ions which rattle in voids.[46] From Rietveld

refinement of our XRD pattern, the phase fraction of the sample is *Pnma* : *Cmcm* 80 : 20. Our experiments are in agreement with previous observations for the *Cmcm* phase, with a lower D_{Li} value of 3.96×10^{-10} cm^2 s^{-1} obtained for the LFP_EG1 sample ($E_{act} = 46$ meV). We can therefore rationalise our ν observations as follows for the LFP_EG1 sample. We continue to observe an increase in ν due to diffusion in the *Pnma* phase, which is present in excess. However, the presence of the *Cmcm* phase acts to limit the supply of Li^+ ions which can diffuse. This impedes the lithium diffusion and results in a lower D_{Li} value.

D Conclusions

We have shown that a microwave-assisted synthetic approach for the preparation of $LiFePO_4$ can allow for different particle morphologies, including crystalline nanoparticles and platelets, and different phases (α- and β-$LiFePO_4$) to be obtained in gram-scale quantities and short reaction times. The microwave dielectric measurements of ethylene glycol and EMI-TFMS reveal these as excellent microwave absorbers to generate the temperatures required for our reactions to proceed. μSR has also proved a powerful tool to examine the Li^+ diffusion in these nanomaterials, with nanocrystalline *Pnma* $LiFePO_4$ exhibiting similar diffusion coefficients to bulk $LiFePO_4$. μSR has also revealed that the presence of the *Cmcm* phase impedes Li^+ mobility and leads to a decrease in Li^+ diffusion. In future, our investigations include varying the experimental conditions to allow for further tuning of the crystal chemistry and morphology, together with additional μSR experiments on mixed metal phosphates.

Acknowledgements

This work was supported by funding from the EPSRC (EP/K029290/1) and Royal Society (RG100301) and we thank the STFC for beamtime allocation. We also acknowledge and thank Prof. J. M. Tarascon for introducing us to the microwave synthesis of $LiFePO_4$ in ionic liquid media.

Notes and references

1 A. K. Padhi, K. S. Nanjundaswamy and J. B. Goodenough, *J. Electrochem. Soc.*, 1997, **144**, 1188.
2 A. K. Padhi, K. S. Nanjundaswamy, C. Masquelier, S. Okada and J. B. Goodenough, *J. Electrochem. Soc.*, 1997, **144**, 1609.
3 J.-M. Tarascon and M. Armand, *Nature*, 2001, **414**, 359.
4 C. Masquelier and L. Croguennec, *Chem. Rev.*, 2013, **113**, 6552.
5 M. S. Whittingham, *Dalton Trans.*, 2008, 5424.
6 A. Manthriam, A. Vadivel Murugan, A. Sarkar and T. Muraliganth, *Energy Environ. Sci.*, 2008, **1**, 621.
7 S. S. Zhang, J. L. Allen, K. Xu and T. R. Jow, *J. Power Sources*, 2005, **147**, 234.
8 R. Dominko, M. Bele, M. Gaberscek, M. Remskar, D. Hanzel, S. Pejovnik and J. Jamnik, *J. Electrochem. Soc.*, 2005, **152**, A607.
9 Z. Lu, H. Chen, R. Robert, B. Y. X. Zhu, J. Deng, L. Wu, C. Y. Chung and C. P. Grey, *Chem. Mater.*, 2011, **23**, 2848.
10 B. Ellis, W. H. Kan, W. R. M. Makahnouk and L. F. Nazar, *J. Mater. Chem.*, 2007, **17**, 3248.
11 J. Zhu, J. Fiore, D. Li, N. M. Kinsinger, Q. Wang, E. DiMasi, J. Guo and D. Kisailus, *Cryst. Growth Des.*, 2013, **13**, 4659.
12 J.-M. Tarascon, N. Recham, M. Armand, J.-N. Chotard, P. Barpanda, W. Walker and L. Dupont, *Chem. Mater.*, 2010, **22**, 724.
13 N. Recham, L. Dupont, M. Courty, K. Djellab, D. Larcher, M. Armand and J.-M. Tarascon, *Chem. Mater.*, 2009, **21**, 1096.
14 P. Barpanda, K. Djellab, N. Recham, M. Armand and J.-M. Tarascon, *J. Mater. Chem.*, 2011, **21**, 10143.
15 I. Bilecka and M. Niederberger, *Nanoscale*, 2010, **2**, 1358–1374.
16 I. Bilecka, A. Hintennach, I. Djerdj, P. Novák and M. Niederberger, *J. Mater. Chem.*, 2009, **19**, 5125.
17 T. Muraliganth, K. R. Stroukoff and A. Manthiram, *Chem. Mater.*, 2010, **22**, 5754.
18 R. Tripathi, G. Popov, X. Sun, D. H. Ryan and L. F. Nazar, *J. Mater. Chem. A*, 2013, **1**, 2990.
19 B. Ellis, L. K. Perry, D. H. Ryan and L. F. Nazar, *J. Am. Chem. Soc.*, 2006, **128**, 11416.
20 P. P. Prosini, M. Lisi, D. Zane and M. Pasquali, *Solid State Ionics*, 2002, **148**, 45.
21 H. Xia, L. Lu and M. O. Lai, *Electrochim. Acta*, 2009, **54**, 5986.
22 A. Eftekhari, *Electrochim. Acta*, 2010, **55**, 3434.
23 L. Lu, *Electrochim. Acta*, 2010, **55**, 3435.
24 D. Morgan, A. Van der Ven and G. Ceder, *Electrochem. Solid-State Lett.*, 2004, **7**, A30.
25 M. S. Islam, D. J. Driscoll, C. A. J. Fisher and P. R. Slater, *Chem. Mater.*, 2005, **17**, 5085.
26 C. A. J. Fisher, V. H. Hart Prieto and M. S. Islam, *Chem. Mater.*, 2008, **20**, 5907.
27 S.-I. Nishimura, G. Kobayashi, K. Ohoyama, R. Kanno, M. Yashima and A. Yamada, *Nat. Mater.*, 2008, **7**, 707.
28 J. Cabana, J. Shirakawa, G. Chen, T. J. Richardson and C. P. Grey, *Chem. Mater.*, 2010, **22**, 1249.
29 C. Delacourt, L. Laffont, R. Bouchet, C. Wurm, J.-B. Leriche, M. Morcrette, J.-M. Tarascon and C. Masquelier, *J. Electrochem. Soc.*, 2005, **152**, A913.
30 S. J. Blundell, *Contemp. Phys.*, 1999, **40**, 175.
31 J. Sugiyama, K. Mukai, Y. Ikedo, H. Nozaki, M. Månsson and I. Watanabe, *Phys. Rev. Lett.*, 2009, **103**, 147601.
32 J. Sugiyama, Y. Ikedo, K. Mukai, H. Nozaki, M. Månsson, O. Ofer, M. Harada, K. Kamazawa, Y. Miyake, J. H. Brewer, E. J. Ansaldo, K. H. Chow, I. Watanabe and T. Ohzuku, *Phys. Rev. B: Condens. Matter Mater. Phys.*, 2010, **82**, 224412.
33 A. S. Powell, J. S. Lord, D. H. Gregory and J. J. Titman, *J. Phys. Chem. C*, 2009, **113**, 20758.
34 A. S. Powell, Z. Stoeva, J. S. Lord, R. I. Smith, D. H. Gregory and J. J. Titman, *Phys. Chem. Chem. Phys.*, 2013, **15**, 816.
35 A. Van der Ven and G. Ceder, *Electrochem. Solid-State Lett.*, 2000, **3**, 301.
36 P. J. Baker, I. Franke, F. L. Pratt, T. Lancaster, D. Prabhakaran, W. Hayes and S. J. Blundell, *Phys. Rev. B: Condens. Matter Mater. Phys.*, 2011, **84**, 174403.

37 J. Sugiyama, H. Nozaki, M. Harada, K. Kamazawa, O. Ofer, M. Månsson, J. H. Brewer, E. J. Ansaldo, K. H. Chow, Y. Ikedo, Y. Miyake, K. Oshishi, I. Watanabe, G. Kobayashi and R. Kanno, *Phys. Rev. B: Condens. Matter Mater. Phys.*, 2011, **84**, 054430.
38 J. Sugiyama, H. Nozaki, M. Harada, K. Kamazawa, Y. Ikedo, Y. Miyake, O. Ofer, M. Månsson, E. J. Ansaldo, K. H. Chow, G. Kobayashi and R. Kanno, *Phys. Rev. B: Condens. Matter Mater. Phys.*, 2012, **85**, 054111.
39 F. J. Douglas, D. A. MacLaren and M. Murrie, *RSC Adv.*, 2012, **2**, 8027.
40 D. M. P. Mingos and D. R. Baghurst, *Chem. Soc. Rev.*, 1991, **20**, 1.
41 A. Sulaimalebbe, A. Porch, F. J. Vidal-Iglesias and G. Attard, *Microwave Symposium Digest, 2008 IEEE-MTT International*, Atlanta, GA, 15–20 June 2008, pp. 1585–1588.
42 D. Slocombe, A. Porch, E. Bustarret and O. Williams, *Appl. Phys. Lett.*, 2013, **102**, 244102.
43 H. Fröhlich, *Theory of Dielectrics*, Clarendon, Oxford, 1958.
44 E. Hanke, K. von Roden and U. Kaatze, *J. Chem. Phys.*, 2006, **125**, 084507.
45 O. García-Moreno, M. Alvarez-Vega, F. García-Alvarado, J. García-Jaca, J. M. Gallardo-Amores, M. L. Sanjuán and U. Amador, *Chem. Mater.*, 2001, **13**, 1570.
46 G. Zeng, R. Caputo, D. Carriazo, L. Luo and M. Niederberger, *Chem. Mater.*, 2013, **25**, 3399.
47 M. Hermanek, R. Zboril, M. Mashlan, L. Machala and O. Schneeweiss, *J. Mater. Chem.*, 2006, **16**, 1273.
48 R. S. Hayano, Y. J. Uemura, J. Imazato, N. Nishida, T. Yamazaki and R. Kubo, *Phys. Rev. B: Condens. Matter Mater. Phys.*, 1979, **20**, 850.